Micro-shimmy of towed structures in experimentally uncharted unstable parameter domain

Dénes Takács [a] & Gábor Stépán [b]

[a] Research Group on Dynamics of Machines and Vehicles, Hungarian
Academy of Sciences, PO Box 91, Budapest, H-1521, Hungary
[b] Department of Applied Mechanics, Budapest University of
Technology and Economics, PO Box 91, Budapest, H-1521, Hungary

Available online: 11 Jun 2012

PLEASE SCROLL DOWN FOR ARTICLE

Taylor & Francis
Taylor & Francis Group

Micro-shimmy of towed structures in experimentally uncharted unstable parameter domain

Dénes Takács[a]* and Gábor Stépán[b]

[a]*Research Group on Dynamics of Machines and Vehicles, Hungarian Academy of Sciences, PO Box 91, Budapest H-1521, Hungary; [b]Department of Applied Mechanics, Budapest University of Technology and Economics, PO Box 91, Budapest H-1521, Hungary*

In this paper, the lateral instability of towed structures (trailers, caravans and articulated buses) is investigated with special attention to the small amplitude lateral vibration that leads to a higher energy consumption in certain parameter domains. A low degree-of-freedom mechanical model of a shimmying towed tyre is used that describes the dynamics of the tyre–ground contact patch by the time delayed differential equation. Stability charts are calculated and the theoretically predicted linear unstable islands of small amplitude shimmy motions are validated by laboratory experiments. A tyre is towed by a relatively long caster, and its temperature and the input current of the conveyor belt are measured in order to show the increased value of the rolling resistance.

Keywords: shimmy; tyre–road interaction; rolling–sliding; thermal effects

1. Introduction

Lateral vibration of towed structures, like the snaking of caravans and trailers, is one of the most dangerous phenomenon of road vehicles. This type of lateral motions can lead to fatal accidents, which explains why the detailed analysis of the lateral stability of road vehicles has always been a relevant research area. The publications [1–5] serve as entry points to the basic literature of the field. A common feature of all these studies is that they consider the mechanical models of both the tyre structure and the tyre–ground contact, which are of different scales. These together with the dynamics of the whole vehicle lead to a multi-scale problem. Tyre models of different levels of complexity are constructed and investigated by several authors and are used in industrial problems as well (see FTire [6], RMOD-K [7], SWIFT [3] and TMeasy [8]). The basic assumptions of the most widely used models are presented and compared to each other in [9].

In another context, the tyre–ground contact dynamics has a key role in the reduction of vehicle noise and rolling resistance. At medium and high speeds of vehicles, the dominant part of the vehicle noise is originated in the tyre [10,11]. In order to reduce the tyre noise, the
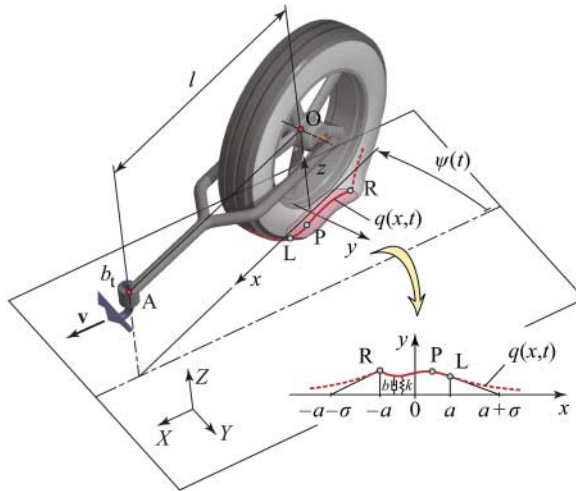

Figure 1.   The mechanical model of towed wheel of elastic tyre.

tyre–ground contact and the related noise generation of tyres are thoroughly analysed in many research reports. For example, experimental studies of tyre noise generation are presented in [12,13]. Regarding the rolling resistance, an essential part of the energy is consumed by the tyres that may warm up heavily. This statement is especially valid in case of heavy vehicles (see [14], as a starting point to the literature survey).

The mechanical model investigated in this paper was introduced and analysed in our former studies [15,16], where the shimmy phenomenon was in focus. With certain limitations, towed structures, like caravans and trailers, especially their lateral stability can also be analysed with the help of the low degree-of-freedom mechanical model shown in Figure 1. Similar models are used in [2,3] and useful practical conclusions are presented. The results of this paper intend to provide observations related to the energy consumption of towed structures as well as to tyre warm-up, wear and noise.

The mechanical model in Figure 1 consists of a wheel of elastic tyre towed by a perfectly rigid suspension system. The king pin (or towing hook) of the towing bar is travelling with a constant velocity and its axis is perpendicular to the ground. This simple one rigid-body degree-of-freedom system is enhanced by the so-called *stretched string tyre model*. The so-called memory effect of tyres was recognised already in [17] but the stability analysis of the exact *stretched string tyre model* became manageable much later as the theory of delay differential equations (DDEs) and bifurcations has developed. This is the reason, why authors like Schlippe and Dietrich [17], Pacejka [3] and other researchers approximated the exact deformation of the tyre by simple functions in the Newtonian equation of motion of the towed wheel. These lead to incomplete linear stability charts but gave simple and practically useful results since the the most relevant stability boundary with respect to towing speed and caster length was determined with good accuracy [18,19]. Moreover, lot of industrial vibration problems were successfully investigated with the help of the tyre models that were developed in these studies. For example, Pacejka's creep force idea is used in [1,20] and von Schlippe's stretched string model is implemented in [21].

The calculation of the stability chart of a towed wheel with exact lateral deformation function (also called *delayed tyre model*) was presented in [22] for tyres of zero relaxation length (*brush model*). An intricate stability chart was obtained with several stable and unstable parameter domains both for short and for long casters. Experiments carried out in [16] emphasised the

importance of stretched string models, where the relaxation length of the tyre was taken into account and a qualitatively similar stability chart was constructed in [15] with fragmented stability domains as obtained for the brush model. This new stability chart predicted the quantitatively reliable parameters of unstable stationary rolling for short caster similarly to Pacejka's creep force model, however, the delayed tyre model predicted instability for long caster, too, where no shimmy was detected by the experiments [3,16].

In this study, the basic equations of the towed wheel with *delayed tyre model* are summarised. The linear stability charts in the plane of towing speed and caster length are constructed for different values of the tyre relaxation length and damping ratio. Simple analytical estimations are given for the unstable parameter domain of long casters. The effect of partial sliding in the tyre contact patch is also taken into account via an extended nonlinear model. It is shown for long caster that the related limitation of the lateral sticking forces in the contact patch reduces the vibration amplitude of the stable periodic shimmy vibration in the most relevant linearly unstable island of the stability chart. Experiments are carried out in order to validate the existence of this numerically detected 'micro-shimmy' motion of the towed structure. A tyre is towed by a relatively long caster, and its temperature and the input current of the conveyor belt are measured in order to show the increased value of a kind of rolling resistance in the unstable parameter domain in question.

2. Mechanical model

A simple low degree-of-freedom mechanical model is presented in Figure 1. The model consists of a wheel of elastic tyre towed by a rigid caster of length l. The caster can rotate around the vertical axis of the king A that is towed by a constant velocity v. The tyre adheres to the ground along the contact patch of length $2a$. The lateral motion of the caster is characterised by the general coordinate ψ. Due to this motion of the caster, the tyre has lateral and longitudinal deformation.

In this study, the lateral deformation is considered only, while the effect of the longitudinal deformation is assumed to be negligible in view of the lateral instability of the trailer. Obviously, this consideration cannot be applied in case of braking or accelerating manoeuvres [3,23], but it leads to acceptable results when the towing velocity is constant. In order to calculate the lateral deformation of the tyre, the so-called *stretched string tyre model* is used [18]. At the time instant t, the tyre forces are calculated with the help of the lateral displacements $q(x, t)$ of tyre centre points identified in the coordinate system (x, y, z) moving together with the caster (Figure 1) and with the help of the specific stiffness k (N/m^2) and the specific damping factor b (Ns/m^2) distributed along the circumference of the tyre. The torsional stiffness at the towing hook is negligible, but it is necessary to model the torsional viscous damping at the bearing with the damping factor b_t (Nms/rad).

2.1. *Governing equations*

The mathematical model is derived in [24] by means of the Appell–Gibbs equations. Without repeating this procedure, we only present the governing equations of this infinite dimensional non-holonomic system with respect to the scalar general coordinate ψ and the distributed (infinite dimensional) one $q(x, .)$.

The first part of the equation of motion is given in the form of an integro-differential equation (IDE):

$$J_A \ddot{\psi}(t) = -b_t \dot{\psi}(t) - \int_{-\infty}^{\infty} (l - x) \left(kq(x, t) + b\frac{\mathrm{d}}{\mathrm{d}t} q(x, t) \right) \mathrm{d}x, \tag{1}$$

where J_A is the mass moment of inertia of the overall system calculated with respect to the z axis at the king pin A. The integral on the right-hand side represents the moment of the tyre forces with respect to the same axis. Dots mean (partial) derivation with respect to time, while d/dt is the material-time derivative. For the explanation of the (approximate) integral limits see [18], where the *stretched string tyre model* was constructed and used first in order to investigate shimmy.

Since we consider rolling, Equation (1) is coupled to the nonlinear partial differential equation (PDE) describing the kinematic constraint of rolling, i.e. the tyre contact points stick to the ground with zero velocity:

$$\dot{q}(x,t) = v \sin \psi(t) + (l-x)\dot{\psi}(t) - q'(x,t)\dot{x}, \tag{2}$$

where $x \in [-a, a]$ and $t \in [0, \infty)$ and the prime denotes differentiation with respect to the space coordinate x. The boundary condition is $q'(a,t) = -q(a,t)/\sigma$, where σ is the so-called relaxation length of the tyre. This condition means that no kink can occur in the lateral tyre deformation at the leading edge L ($x = a$) [3]. The kinematic constraint of rolling gives also the longitudinal translational speed of the tyre points:

$$\dot{x} = -v \cos \psi(t) + q(x,t)\dot{\psi}(t), \tag{3}$$

which simplifies to $\dot{x} \approx -v$ in case of small oscillations, i.e. when $\psi(t)$ and $q(x,t)$ are small. This translational speed Equation (3) appears in the linearised form of the PDE Equation (2):

$$\dot{q}(x,t) = v\psi(t) + (l-x)\dot{\psi}(t) + vq'(x,t). \tag{4}$$

The lateral deformation of the tyre outside the contact patch ($x < -a$ or $x > a$) is approximated by exponential decay functions in correspondence with the *stretched string tyre model*, namely:

$$q(x,t) = \begin{cases} q(-a,t)\,\mathrm{e}^{(x+a)/\sigma}, & \text{if } x \in (-\infty, -a), \\ q(x,t), & \text{if } x \in [-a,a], \\ q(a,t)\,\mathrm{e}^{-(x-a)/\sigma}, & \text{if } x \in (a, \infty). \end{cases} \tag{5}$$

Using these functions in Equation (1), the integral can be separated into three parts, and only the contact range ($-a \le x \le a$) remains unknown, while the other parts can be calculated in the closed form.

2.2.   *Memory effect of tyres*

As it was mentioned in Section 1, it was already recognised by von Schlippe in 1941 (see [17]) that the longitudinal translation of the tyre particles provides a kind of memory in the tyre. Namely, an actual wheel position is stored by the absolute position of the tyre particle that touches the ground at the leading point L ($x = a$) of the contact patch and travels backwards relative to the caster as the wheel rolls ahead. The wheel position is kept in memory until the particle reaches the trailing edge R ($x = -a$). This translation needs approximately the time period $2a/v$ if a small tyre deformation and small caster angle are considered.

Thus, the time delay

$$\tau(x) \approx \frac{a-x}{v}, \quad x \in [-a,a] \tag{6}$$

can be introduced in case of small oscillations, which time is needed for a tyre particle to travel backward relative to the caster from the leading edge L ($x = a$) of the contact patch to

its actual position x. By means of this delay, a travelling wave solution of the linearised PDE Equation (4) can be obtained in the form (see [15] for details):

$$q(x, t) = (l - a + v\tau(x))\psi(t) - (l - a)\psi(t - \tau(x)) + q(a, t - \tau(x)) \tag{7}$$

for $x \in [-a, a]$. This way, the IDE–PDE coupled system Equations (1)–(3) can be simplified into a (linear) system of a DDE with distributed and discrete delays coupled to an ordinary differential equation. We present these after introducing dimensionless parameters.

2.3. *Rescaling and dimensionless parameters*

At zero speed ($v = 0$), the angular natural frequency of the structure is

$$\omega_{\mathrm{n}} = \sqrt{\frac{2k}{J_{\mathrm{A}}} \left(a \left(l^2 + \frac{a^2}{3} \right) + \sigma(l^2 + a^2 + a\sigma) \right)} \tag{8}$$

and the damping ratio has the form

$$\zeta = \frac{1}{2\omega_{\mathrm{n}}} \left(\frac{2b}{J_{\mathrm{A}}} \left(a \left(l^2 + \frac{a^2}{3} \right) + \sigma(l^2 + a^2 + a\sigma) \right) + \frac{b_{\mathrm{t}}}{J_{\mathrm{A}}} \right). \tag{9}$$

These modal parameters introduce the dimensionless towing speed, caster length, relaxation length and torsional damping as

$$V := \frac{1}{\omega_{\mathrm{n}}} \frac{v}{2a}, \quad L := \frac{l}{a}, \quad \Sigma := \frac{\sigma}{a}, \quad B := \frac{b_{\mathrm{t}}}{2a^3 b}, \tag{10}$$

respectively.

Introduce also the dimensionless time $T = (v/2a)t$, the integration variable $\vartheta = -(v/2a)\tau$ and the dimensionless leading point lateral displacement $Q(T) = q(a, T)/a$. Then, the usual Cauchy transformation of the linearised IDE–PDE Equations (1)–(3) leads to a three-dimensional system of first-order DDEs

$$\begin{pmatrix} \dot\psi(T) \\ \dot\Omega(T) \\ \dot Q(T) \end{pmatrix} = \begin{pmatrix} 0 & 1 & 0 \\ -\dfrac{1}{V^2} + c_1 & -\dfrac{2\zeta}{V} & -c_2 \dfrac{\Sigma}{2}(L - 1 - \Sigma) \\ 2 & L - 1 & -\dfrac{2}{\Sigma} \end{pmatrix} \begin{pmatrix} \psi(T) \\ \Omega(T) \\ Q(T) \end{pmatrix}$$

$$+ c_2 \int_{-1}^{0} (L - 1 - 2\vartheta) \begin{pmatrix} 0 & 0 & 0 \\ L - 1 & 0 & -1 \\ 0 & 0 & 0 \end{pmatrix} \begin{pmatrix} \psi(T + \vartheta) \\ \Omega(T + \vartheta) \\ Q(T + \vartheta) \end{pmatrix} d\vartheta + \frac{L + 1 + \Sigma}{2}$$

$$\times \begin{pmatrix} 0 & 0 & 0 \\ (L - 1)(c_2 \Sigma - 2c_3) - 2c_3 \Sigma & 0 & -c_2 \Sigma + 4c_3 \\ 0 & 0 & 0 \end{pmatrix} \begin{pmatrix} \psi(T - 1) \\ \Omega(T - 1) \\ Q(T - 1) \end{pmatrix}, \tag{11}$$

with the parameters

$$c_1 = c_2 \frac{\Sigma}{2}(L - 1 - \Sigma)(L - 1) + c_3(L^2 + (1 + \Sigma)^2),$$

$$c_2 = \frac{1}{V^2} \frac{1}{L^2 + 1/3 + \Sigma(L^2 + 1 + \Sigma)}, \tag{12}$$

$$c_3 = \frac{2\zeta}{V} \frac{1}{L^2 + 1/3 + \Sigma(L^2 + 1 + \Sigma) + B}.$$

3.   Unstable parameter domains

The stationary rolling of the wheel is represented by the trivial solution

$$\begin{pmatrix} \psi(T) \\ \Omega(T) \\ Q(T) \end{pmatrix} \equiv \mathbf{0}. \tag{13}$$

The Laplace transformation of Equation (11) or the substitution of the trial solution $\mathbf{K}\,e^{\lambda T}$ ($\mathbf{K} \in \mathbb{C}^3$ and $\lambda \in \mathbb{C}$) leads to the characteristic function

$$
\begin{aligned}
D(\lambda) = {} & V^2 \Sigma \lambda^3 + (2V^2 + 2\zeta V \Sigma)\lambda^2 + (\Sigma + 4\zeta V)\lambda \\
& - \frac{4\zeta VL(\Sigma + 1)(\Sigma\lambda + 2)}{L^2 + 1/3 + \Sigma(L^2 + 1 + \Sigma) + B} + 2 \\
& - \frac{L - 1 - \Sigma}{L^2 + 1/3 + \Sigma(L^2 + 1 + \Sigma)} \\
& \times \left\{ \Sigma(e^{-\lambda} - 1 + L(e^{-\lambda} + 1) + \Sigma(e^{-\lambda} - 1)) \right. \\
& \left. + \frac{2}{\lambda}\left(\left(L - 1 + \frac{2}{\lambda}\right) - \left(L + 1 + \frac{2}{\lambda}\right)e^{-\lambda} \right) \right\} \\
& - \frac{2\zeta V(L - 1 - \Sigma)}{L^2 + 1/3 + \Sigma(L^2 + 1 + \Sigma) + B} \\
& \times \{ \Sigma\lambda(e^{-\lambda} - 1 + L(e^{-\lambda} + 1) + \Sigma(e^{-\lambda} - 1)) \\
& - 2(e^{-\lambda} + 1 + L(e^{-\lambda} - 1) + \Sigma(e^{-\lambda} + 1)) \}.
\end{aligned} \tag{14}
$$

This transcendental function has infinitely many (complex) zeros for the characteristic exponents (characteristic roots) λ, and the stationary rolling is asymptotically stable if and only if all the characteristic exponents are situated in the left-half complex plane [25]. At the limit of stability, bifurcation can take place in the corresponding nonlinear system as the characteristic roots cross the imaginary axis for some critical values of the parameters.

Saddle-node (SN) bifurcation (static loss of stability) of the stationary rolling may take place when a real characteristic exponent crosses the imaginary axis. The characteristic function is defined by its continuous extension for $\lambda \to 0$:

$$D(0) = 2 - \frac{2L(L - 1 - \Sigma)(\Sigma + 1)}{L^2 + 1/3 + \Sigma(L^2 + 1 + \Sigma)} - \frac{8\zeta V(\Sigma + 1)^2}{L^2 + 1/3 + \Sigma(L^2 + 1 + \Sigma) + B}. \tag{15}$$

The stability boundary related to the SN bifurcation can be calculated from $D(0) = 0$, which leads to the stability limit $L_{\mathrm{SN}} = -1/3$ in case of zero relaxation length ($\Sigma = 0$) and zero damping ($\zeta = 0$ that also means $B = 0$). This stability boundary is also identified in case of mechanical models with a different tyre model [3]. This static loss of stability has no further relevance in this study since it appears only for pushed wheels (see the stability chart in Figure 2).
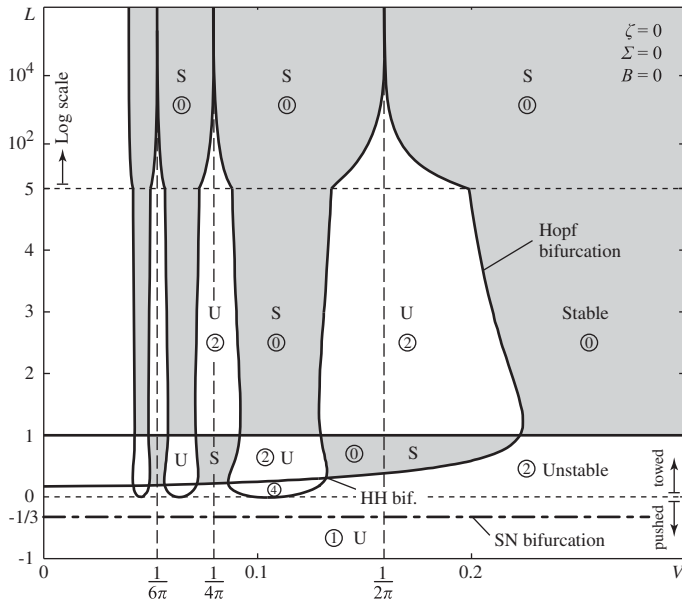
Figure 2. The stability chart of the undamped system for $\Sigma = 0$. Stability boundaries are plotted by a thick solid line. Stable domains are shaded. The encircled numbers mean the number of the characteristic roots with positive real parts. Logarithmic scale is applied in the chart for $L > 5$. The asymptotes of the stability boundaries for $L \to \infty$ are marked by dashed lines.

In case of the dynamic loss of stability, Hopf bifurcation occurs as a pair of pure imaginary complex conjugate characteristic exponents cross the imaginary axis at $\lambda_{1,2} = \pm i\omega$ with the dimensionless angular frequency ω of the emerging self-excited vibrations. The corresponding stability boundaries can be determined by the D-subdivision method in the parameter space. The characteristic exponent $\lambda_1 = i\omega$ is substituted into Equation (14) and $D(i\omega)$ is separated to real and imaginary parts: Re $D(i\omega) = 0$ and Im $D(i\omega) = 0$.

The resulting stability chart of the undamped system ($\zeta = 0$) for zero relaxation length ($\Sigma = 0$) is shown in Figure 2, where $\omega \in [0, 8\pi]$ and the stable parameter domains are shaded. The encircled numbers show the number of the unstable characteristic roots. Notice that there exists a stability boundary at $L = 1$, and for large V the system is stable above this boundary and unstable below. For $L \to \infty$, the asymptotes of the Hopf bifurcation boundaries are characterised by

$$V_{\text{cr}} = \frac{1}{2j\pi}, \quad \text{where } j = 1, 2, 3, \ldots, \tag{16}$$

which are also marked in Figure 2 with dashed vertical lines. As it can be observed in the corresponding stability chart, there are large unstable islands around these critical values of the towing speeds even for very long caster lengths. The algebraic explanation of the above properties of the stability chart is given in [22] in detail.

The effect of the non-zero relaxation length Σ is presented in Figure 3. The relaxation of the tyre amplifies the whole stability chart together with the stable and unstable domains. For example, the critical stability boundary $L = 1$ is shifted to the boundary at $L = 1 + \Sigma$: above this line, the stationary rolling is stable for large values of V. For $L \to \infty$, the characterising critical towing speeds V_{cr} of the asymptotes of the Hopf bifurcation boundaries cannot be determined analytically. Still, it is easy to calculate their numerical values as a function of the relaxation length Σ as shown in the lower panel of Figure 3 for the first value
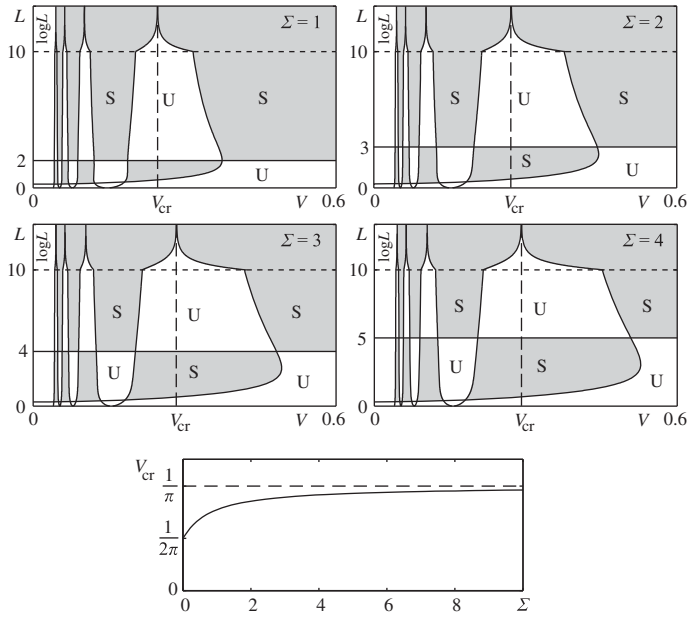
Figure 3.   The stability chart of the undamped system for different values of the relaxation length Σ. Logarithmic scale is applied in the charts for $L > 10$. The asymptote is marked by a dashed line, which characterises the most relevant unstable island of caster lengths $L > 1 + \Sigma$. The corresponding critical towing speed V_{cr} is plotted against the relaxation length Σ in the lower panel.

($j = 1$). This characterises the asymptote of the most relevant linearly unstable island for large caster lengths, which is also marked by vertical dashed lines in the stability charts. The asymptote tends to $V_{cr} \to 1/\pi \approx 0.318$ when $\Sigma \to \infty$. This means that the relevant unstable island can exist near to and around the parameter domain $L > 1 + \Sigma$ and $1/(2\pi) \leq V \leq 1/\pi$, i.e. for

$$l > a + \sigma \quad \text{and} \quad \frac{a\omega_n}{\pi} \leq v \leq \frac{2a\omega_n}{\pi}. \tag{17}$$

The effect of damping is represented in Figure 4, where the stability charts are constructed for different damping ratios and for a realistic dimensionless relaxation length $\Sigma = 2$. The stability boundaries are shown by thick lines while the stability boundaries of the undamped system are also illustrated by thin lines. The effect of damping is clear: the greater the damping is, the smaller are the unstable domains. This is well-known in practice, consequently, shimmy dampers are often applied on motorcycles [26] and at air plane nose gears. For large enough damping, only the most relevant unstable domain survives, which was also detected in several different studies on shimmy [3,17,18,27], but the manoeuvrability of the system is severely reduced.

The exact analysis of the *stretched string tyre model* locates many unstable stability domains of the towed wheel, which can also be important in practice. See [16], for example, where experimentally detected quasi-periodic vibrations are explained by this simple one rigid-body degree-of-freedom mechanical model extended by the delayed tyre model. These vibrations also verified the existence of the unstable islands below $L = 1 + \Sigma$. In what follows, we study the unstable islands for long casters $L > 1 + \Sigma$ and verify their existence experimentally especially in case of the rightmost one.
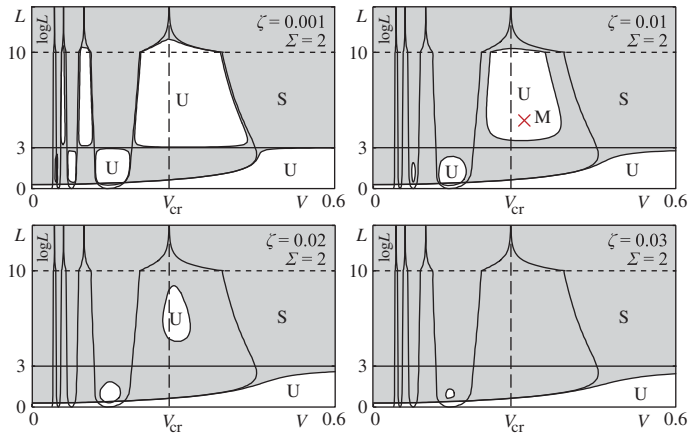
Figure 4. The stability chart of the towed structure for different values of the damping ratio ζ. Stability boundaries of the damped system are drawn by thick lines while the thin lines are the stability boundaries of the undamped system. Cross marks for the parameter point M that is used in Section 4. Logarithmic scale is applied in the charts for $L > 10$. The asymptote is marked by a dashed line, which characterises the most relevant unstable island of caster lengths $L > 1 + \Sigma$.

4. Nonlinear effect of sliding

An alternative way to investigate the dynamics of the towed wheel of elastic tyre is the numerical simulation of the IDE–PDE system Equations (1)–(3). With the help of the analytically determined stability diagrams, we also validate the applied numerical methods. On the other hand, numerical simulation provides new information about the arising nonlinear (self-excited) oscillations in the predicted unstable parameter domains, moreover, it can confirm or deny the relevance of the existence of these unstable islands; this way it also guides us as to how to detect the islands experimentally.

In the numerical simulation code, a third order Runge–Kutta method was adapted for the time domain, while the finite difference method was applied for the space discretisation with respect to x. The time step and the number of the spatial mesh points were tuned together in order to fulfil the so-called Courant–Friedrichs–Lewy stability condition [28]. Namely, the number of the mesh points were $n = 100$ and the time step was calculated from the towing speed with the empirical formula: $\Delta t = 2a/(20v(n-1))$.

Simulations often show unrealistically large tyre deformations for stable periodic oscillations, which obviously violates the sticking condition; in practice, sliding of certain tyre points occurs. Accordingly, our laboratory experiments showed discrepancies compared to simulation results where geometric nonlinearities were included only and the static coefficient of friction μ_s was set to infinity. This convinced us about the key (nonlinear) role of partial sliding of the tyre particles in the contact patch during the large amplitude nonlinear oscillations.

Thus, we used the equations of motion Equation (1) and the kinematic constraint Equation (2), together with checking the maximum possible lateral forces in the contact patch prescribed by a realistic value of the static coefficient of friction μ_s. We implemented the so-called extended Coulomb friction model in our simulation code, which is the simplest (non-smooth) approximation of frictional contact forces. As explained in Section 2, we do not consider the longitudinal deformation of the tyre and corresponding longitudinal distributed forces, which would be essential if we investigated the dynamics of braking or accelerating.

In order to calculate the critical (maximal) lateral forces, we use a parabolic function to approximate the normal force distribution in the contact patch, which was developed by Pacejka [19] during a simplified derivation of the creep–force idea. The critical lateral forces and the sliding friction forces are described by

$$p_{cr}(x) = \frac{3}{4}\mu_s \frac{F_z}{a}\left(1 - \frac{x^2}{a^2}\right) \tag{18}$$

and

$$p_d(x) = \frac{3}{4}\mu_d \frac{F_z}{a}\left(1 - \frac{x^2}{a^2}\right), \tag{19}$$

respectively, where F_z is the resultant (constant) normal force between the tyre and the ground and μ_d is the dynamic coefficient of friction.

During the vibration of the tyre, we should decide whether the tyre starts partially sliding or not, namely, we should calculate the actually required lateral force distribution in the contact patch, which would be needed to hold the actual deformed shape of the stretched string. If the inertia of the tyre particles is negligible, this can be done by means of the differential equation of the stretched string:

$$\dot{q}(x,t) + q'(x,t)\dot{x} - \frac{k}{b}\sigma^2 q''(x,t) + \frac{k}{b}q(x,t) = \frac{p(x,t)}{b}, \tag{20}$$

where $p(x,t)$ is the lateral force distribution acting on the stretched string and $\dot{x}$ is given by Equation (3). For the derivation of Equation (20) see [29] in case of zero damping. Thus, the required lateral force distribution is

$$p_{req}(x,t) = k(q(x,t) - \sigma^2 q''(x,t)) + b(\dot{q}(x,t) + q'(x,t)\dot{x}). \tag{21}$$

If this required lateral force of a tyre point at position x reaches the critical lateral force, i.e. if $p_{req}(x,t) > p_{cr}(x)$, the corresponding tyre element starts sliding, the kinematic constraint of rolling is relaxed, and Equation (2) is not fulfilled until the tyre point sticks again to the ground. The lateral velocity of this sliding tyre point P relative to the ground is

$$v_{Py}(x,t) = -v\sin\psi(t) - (l-x)\dot{\psi}(t) + \dot{q}(x,t) + q'(x,t)\dot{x}. \tag{22}$$

The lateral displacement of these sliding tyre points, i.e. their lateral deformation $q(x,t)$ during the sliding, is described by the differential equation (20) of the damped stretched string, where the lateral force is $p(x,t) = -\text{sign}(v_{Py}(x,t))p_d(x)$. For the rest of the sticking tyre points, which satisfy the conditions $p_{req}(x,t) \leq p_{cr}(x)$ and $v_{Py}(x,t) = 0$, the PDE (2) is still valid.

The boundary conditions of Equation (20) are chosen by means of the configuration of the actual sliding zones within the contact patch. If a sliding zone does not reach the ends of the contact patch, the continuity of the lateral deformation function $q(x,\cdot)$ gives two Dirichlet boundary conditions. If the sliding zone contains the rear and/or the leading point of the contact patch, the mixed boundary conditions $q'(-a,t) = q(-a,t)/\sigma$ and/or $q'(a,t) = -q(a,t)/\sigma$ are valid, respectively. These cases originated from the fact that the lateral forces are zeros at R and L and they vary continuously at these points. This also means, that the so-called 'no kink at L' condition [3] has to be extended generally with the 'no kink at R' condition if (partial) sliding is considered in the model.

The simulation of the above described nonlinear system requires an adequate time step, which is much smaller when sliding is taken into account as compared to case of pure rolling. Since the dynamics of sliding in the contact patch is one range faster than the dynamics of

Table 1. The system parameters used for the simulation at the parameter point M.

Dimensional parameters		Dimensionless parameters	
v (m/s)	0.2978	V	0.3
l (m)	0.1975	L	5
σ (m)	0.079	Σ	2
$2a$ (m)	0.079	B	0
J_A (kgm^2)	3.9742	ζ	0.01
k (kN/m^2)	62.6		
b (Ns/m^2)	99.63		
b_t (Nms/rad)	0		
ω_n (rad/s)	4π		
F_z (N)	200		
μ_s (–)	1.0		
μ_d (–)	0.7		

the rigid-body system, the satisfaction of the Courant–Friedrichs–Lewy stability condition requires one thousandth of the former time step, which increases the computational effort tremendously.

This observation required the application of the following simplification in the simulation code. We simulate the original equations Equations (1)–(3) with the original time step that was applied for the rolling case ('slow' dynamics), and we check the lateral force distribution after each time step. If sliding occurs in the contact patch, we posteriorly modify the lateral deformation function $q(x, \cdot)$ by means of the simulation of the PDE (20) ('fast' dynamics) with the decreased time step. Meanwhile the simulation time of the main dynamics is stopped, and the caster angle and the angular velocity are kept constant. This means that the lateral deformation function jumps to a new shape infinitely fast. This technique is often used during the simulation of multiscale problems.

Long series of simulations were carried out in [30] for different parameter points of the stability charts. Some of them were also validated by experiments for short casters ($L < 1 + \Sigma$). This time, we investigate the upper ($L > 1 + \Sigma$) unstable island and present simulations at the parameter point M (marked by a cross in Figure 4) only, with and without partial sliding in the contact patch. For both cases, the same initial condition is used, i.e. $\psi(0) = 0$, $q(x, 0) \equiv 0$ and $\dot{\psi}(t) = -2$ rad/s. The system parameters at the parameter point M are shown in Table 1 both in a dimensional and in a dimensionless form. The numerical values of the parameters F_z, μ_s and μ_d characterising the lateral force distributions in Equations (18) and (19) are set at realistic values.

5. Simulation results

The results are shown in Figure 5. Panel (a) corresponds to the original model without the nonlinear effect of sliding. The time history of the caster angle $\psi(t)$ is shown together with the lateral deformation function $q^*(x) = q(x, t^*)$ at the optionally chosen time instant t^*. The location of the king pin A is also marked in the figure in order to illustrate the structure of the towed wheel having a centre at zero. Due to the geometric nonlinearities in the system, the motion tends to a stable periodic solution having an amplitude somewhat less than $\pi/4$. The lateral deformation of the tyre at the detected periodic solution is quite large at t^*, it almost reaches 100 mm.
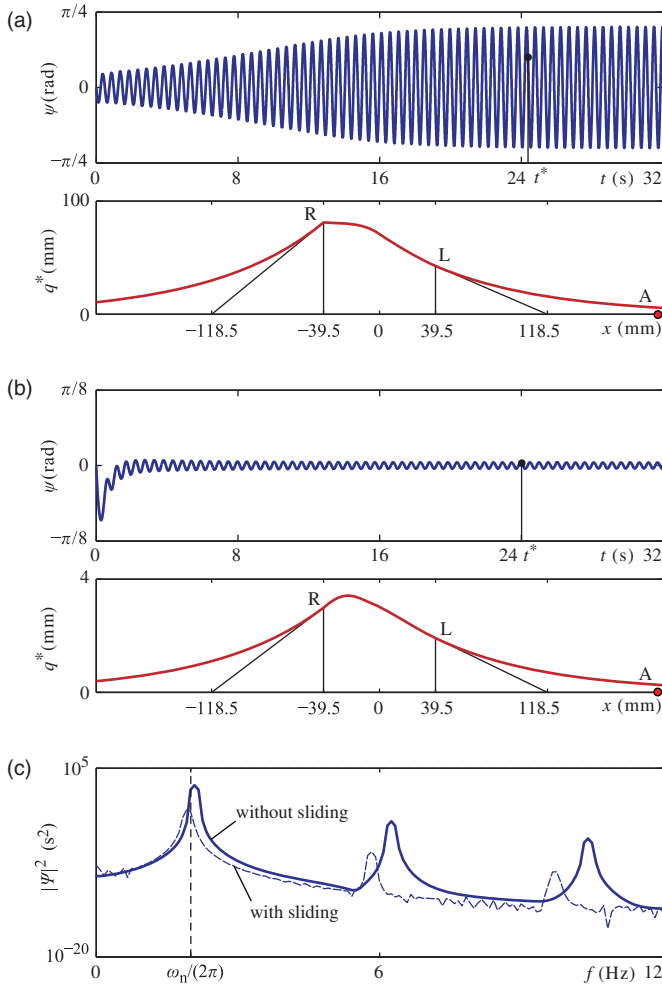
Figure 5. Simulation results at the parameter point M. Panel (a) shows the time history of the caster angle and the tyre deformation function at the time instant $t^\star$ when sliding effect is not considered. Panel (b) shows the results in case of sliding. The spectra of the time signals are plotted in panel (c) for both cases.

The time history and the lateral deformation function in Figure 5(b) corresponds to the simulation with the nonlinear effect of partial sliding. The amplitude of the stable periodic motion is much smaller, namely, it is less than $0.016\,\text{rad} = 0.92°$. The lateral deformations within the tyre contact patch show the same reduction of the oscillations. This is due to the fact that the kink at the rear point R cannot appear since the lateral force distribution should always be zero at R, and the rear part of the contact patch always slides. This effect does not allow the evolution of such large amplitude vibrations that are shown in panel (a). All this means, that almost invisible vibrations occur only in spite of the fact that the stationary rolling is (linearly) unstable.

The spectra of the last 12 s of the simulated oscillations are compared in Figure 5(c). A small variation of the basic frequencies can be observed, namely, the basic frequency is somewhat smaller if sliding is taken into account. In both cases, these are close to the natural frequency $(f_\text{n} = \omega_\text{n}/(2\pi))$ of the structure in accordance with the analytically determined self-excited vibration frequencies at the Hopf bifurcation boundaries (see details in [30]).
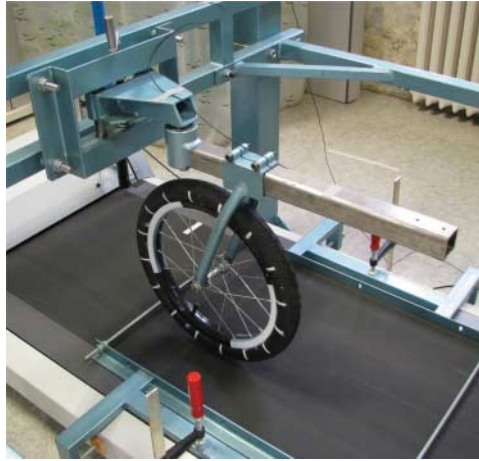
Figure 6.   The experimental rig.

6.   Experimental setup

An experimental rig was designed and built in order to carry out a long series of experiments. The rig is described in details in [30]. The wheel used in the experiments is originally part of a small bicycle, and it is towed by a special suspension system fixed above a conveyor belt as shown in Figure 6. The suspension system corresponds exactly to the mechanical model shown in Figure 1, consequently, it keeps the plane of the wheel perpendicular to the ground.

Several experiments were carried out in different parameter domains of the stability chart in Figure 4. The most relevant stability boundary was clearly detected in the lower part of the chart (for $L < 1 + \Sigma$) together with the quasi-periodic oscillations at the intersections of the relevant stability boundary and the lower unstable islands (see details in [16,24]). However, the linearly unstable parameter domains (islands) for a long caster were not observable experimentally based on the measured vibration signals, which showed only the tiny background noise for all the parameters $L > 1 + \Sigma$. Since the relevance of the memory effect in tyres could unquestionably be confirmed by the validation of at least the largest unstable island, further experiments were carried out at the corresponding parameters. The initiation of this additional series of experiments were also encouraged by the modal testing results presented in [31], where the critical pair of complex characteristic roots in the unstable parameter island were clearly identified by the impact experiments carried out during rolling.

One explanation for the non-observability of the self-excited oscillations in the linearly unstable parameter domain might be that the amplitude of the vibrations is limited by the nonlinear effect of sliding so much that the vibration remains hidden by the noise of the measured signals. Still there exists a maximum lateral force distribution in the contact patch within which the vibrations can increase without the sliding of tyre points. When the lateral force distribution in the contact patch reaches this maximum value somewhere within the contact patch, the corresponding tyre points start sliding and the vibrations decay in time till the sliding is completed, then the tyre points stick again, and the vibrations can start increasing again. In the unstable island, this effect leads to a small (practically invisible) self-excited vibration with several microslips in the contact patch.

This was recognised during the analysis of the numerical simulations described in Section 4. Although the vibrations are small, the microslips dissipate most of the mechanical energy
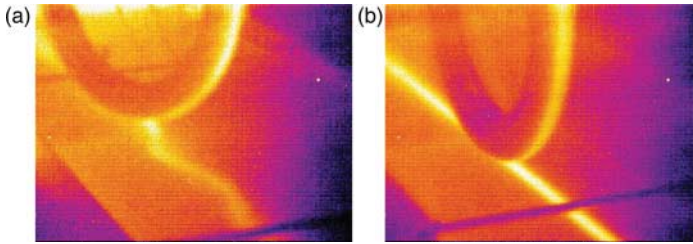
Figure 7. Pictures made by the thermal camera at different parameter points.

introduced by the self-excited shimmy vibration. This means that it is 'more difficult' to pull the wheel in these parameter regions, namely, the resistance to rolling has a higher level in these unstable parameter domains of shimmying wheels. As a consequence of the above described effect, the tyre may warm up to a somewhat higher temperature, and the wear of the tyre may speed up in these parameter domains while the shimmy vibration itself can be observed neither visually nor with sophisticated dynamic measurement systems due to the presence of noise.

The above described power dissipation of the wheel shimmy was verified experimentally in the unstable parameter island when the temperature of the tyre and the electric input current of the conveyor belt were measured. After fixing all of the system parameters, the towing speed was tuned to a desired value within and around the unstable island, and the tyre was run for some minutes at the same speed in order to reach the stationary temperature distribution. Then, the temperatures of the tyre was measured by a pyrometer. The resolution of the pyrometer was $1°C$. The generation of heat was also observed by a sensible thermal camera in order to verify the locations of the power dissipation. Two pictures are shown in Figure 7 in order to demonstrate that the generation of heat has a measurable level and the thermal camera was able to visualise the wheel–track in real time. The average of the input current of the conveyor belt was also recorded by an electric-supply metre with the resolution of 0.01 A.

In Figure 7(a), the wheel–track is shown in an unstable domain for short caster parameters, where the vibrations are also clearly observable along with the local temperature increase. The normal load on the tyre generates normal forces and related friction forces between the belt and the supporting plate below the belt. The work of the friction forces heats the belt and the belt also heats the tyre even in case of stable stationary rolling without microslips. This was confirmed by the thermal camera (Figure 7(b)). Unfortunately, this effect makes the verification of the microslips even more difficult. Nevertheless, the power dissipation of the friction forces between the belt and the supporting plate depends linearly on the towing speed, while the power dissipation of the microslips should occur in a certain speed range only. If the towing speed is chosen from the prescribed speed range of the unstable island, higher temperatures and higher electric input current should be measured.

7. Measurement results

The system parameters of the experimental setup are given in Table 2, and the corresponding experimental results are presented in Figure 8. In panel (a), the dimensional form of the theoretical stability chart is constructed in the (v, l) plane for the experimental parameter configuration in question. The analytically determined asymptotes are also illustrated with dashed lines in order to show that formula (17) can efficiently help to locate the upper unstable

Table 2. The system parameters in the experimental setup.

Dimensional parameters		Dimensionless parameters	
v (m/s)	0.14 … 5	V	0.07 … 2.68
l (m)	0.300	L	7.60
σ (m)	0.130	Σ	3.29
$2a$ (m)	0.079	B	260
J_A (kgm^2)	3.6132	ζ	0.007
k (kN/m^2)	62.6		
b (Ns/m^2)	19		
b_t (Nms/rad)	0.61		
ω_n (rad/s)	23.65		
F_z (N)	180		
μ_s	1.5		
μ_d	1.0		

island in practice. In panel (b), the common real part of the theoretically calculated relevant (rightmost) characteristic root is plotted for $l = 0.3$ m against the towing speed.

The fully developed shimmy oscillations were simulated for different values of the towing speed, and the bifurcation diagram of the system was partially conjectured. This bifurcation diagram is shown in panel (c), where the numerically calculated stable branch is represented by a (green) solid line, while the hypothetic unstable periodic branch is illustrated by a (red) dashed line. It seems to be a non-conventional supercritical Hopf bifurcation at $v = 0.75$ m/s in the sense that it does not follow the standard parabola shape. This is common, however, for bifurcations in the non-smooth systems with the Coulomb friction as shown in [32] for stick–slip tasks. It is likely that the subcritical Hopf bifurcation at $v = 0.44$ m/s is also degenerate in the same way. The exact bifurcation analysis of the system at these parameter points is an exciting challenge for future mathematical research.

In Figure 8, panel (d) shows the actual temperature of the tyre at the trailing edge, while panel (e) shows the increments of the electric current that were measured between two cases: first, the conveyor belt ran with the wheel on it; second, it ran free of the wheel that was lifted up. The measurement points are presented by (blue) crosses in these panels. A higher level of the temperature can clearly be observed at the towing speeds 0.25–0.6 m/s, which perfectly coincides with the region where the stable periodic vibrations were predicted with microslips, while the linearly unstable speed range is predicted for the somewhat higher towing speed region 0.44–0.75 m/s. As explained above, the shift between the observed and the predicted critical speed ranges is a straightforward consequence of the bifurcation diagram in panel (c). The numerical bifurcation analysis of the system shows that the largest amplitude vibrations of the towed wheel and consequently the largest gradient in the temperature increase may appear somewhat 'before' the unstable island of the stability chart, where the linearly stable stationary rolling coexists with the tiny stable periodic motion with microslips.

The electric current in panel (e) also shows a definite local maximum in the same critical speed range. It must be mentioned, however, that the characteristics of the electric motor driving the conveyor belt could not be identified and the dashed line in panel (e) illustrates only the estimated power requirement caused by the friction forces between the belt and the plastic plate under the belt. A certain percentage of the power increments in the range of the increased current may also be related to the change in the efficiency of the motor at different speeds, but still, a relevant part of this power increment must be related to the temperature increase of the tyre through the microslips caused by the tiny shimmy motion.

These measurement results confirm the existence of the linearly unstable island in the stability chart for long caster where the self-excited vibration has so small an amplitude due
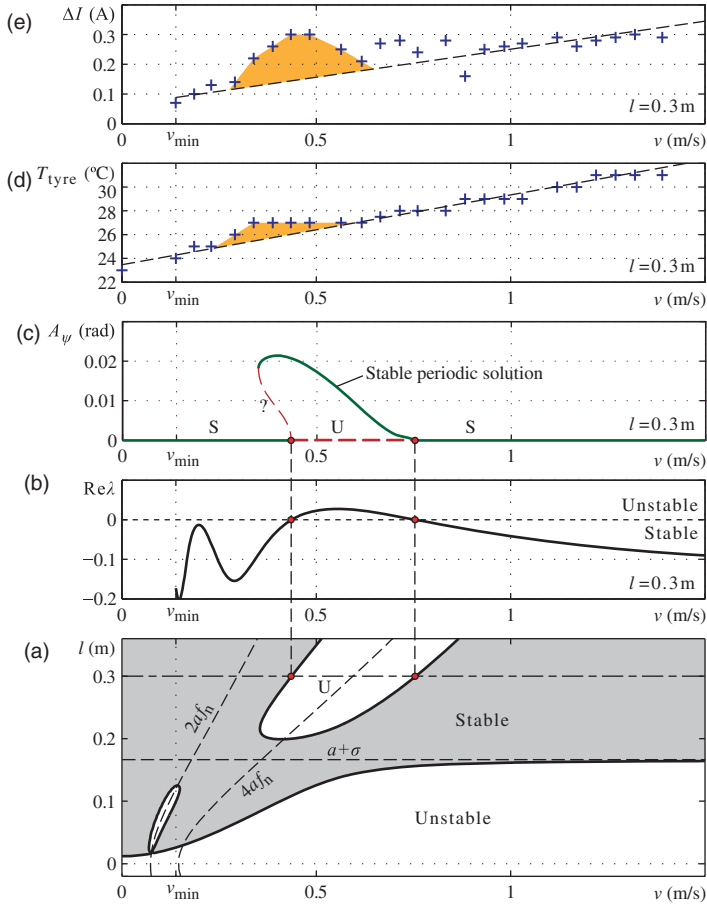
Figure 8. Heat generation of micro-shimmy. Panel (a) shows the theoretical stability chart for the experimental parameter configuration. In panel (b), the real part of the theoretically calculated relevant characteristic root is plotted against the towing speed. Panel (c) shows the bifurcation diagram at the fixed caster length. Panels (d) and (e) present the actual temperature of the tyre at the tyre trailing edge and the measured increments of the electric current, respectively.

to the microslips that it cannot be distinguished from the background noise in the system. This explains the introduction of the idea of 'micro-shimmy'.

8. Conclusion

A low degree-of-freedom mechanical model of the shimmying towed wheel was considered with the exact *stretched string tyre model*. The mathematical model of the towed wheel of the elastic tyre was given in the form of a coupled IDE–PDE system, which was transformed into a system of the first-order DDEs, where the time delay is originated in the memory effect of the contact patch. The theoretical linear stability chart of the stationary rolling was constructed for different sets of the model parameters. It was shown that experimentally uncharted unstable parameter domains exist related to the memory effect of the tyre.

The nonlinear effect of the partial sliding in the contact patch was taken into account that leads to a 'fast' and to a 'slow' dynamical subsystem. An approximation of this multi-scale problem was applied in order to reduce the computational effort of the simulation process.

It was shown that the sliding in the contact patch eliminates the large amplitude periodic shimmy oscillation in the experimentally uncharted linearly unstable parameter domain and it results the so-called 'micro-shimmy' of the towed wheel. The location of the uncharted unstable domain was estimated with the help of the analytically determined asymptotes of the linear stability boundaries. Namely, the relevant unstable island can exist around the parameter domain:

$$l > a + \sigma \quad \text{and} \quad 2af_\mathrm{n} \leq v \leq 4af_\mathrm{n}, \tag{23}$$

where f_n is the natural frequency of the caster-wheel system in Hertz at zero towing speed. Notice that this estimation is coming from a simple one rigid-body degree-of-freedom mechanical model of the towed structure and its validity can be questioned for more complex systems.

Although, this 'micro-shimmy' vibration can hardly be detected by means of dynamic measurements, its practical relevance is unquestionable since it causes increased resistance to rolling, increased thermal load and increased wear of the tyre. Since the rolling resistance consumes substantial energy, simple adaptive control strategies may help to reduce tyre wear, fuel consumption and tyre noise via avoiding these critical towing speed ranges. It is also important to know that the efficiency of ABS is reduced for these towing speed domains due to the many fractional microslips within the contact patch.

The phenomenon 'micro-shimmy' can be useful at the testing procedure of newly developed tyre models. Namely, sophisticated tyre models that are efficiently used in complex industrial problems should also be able to identify those critical parameter domains, which are predicted and verified by our simple mechanical model and experiments. For example, a comparison of the widely used tyre models, such as FTire [6], RMOD-K [7], SWIFT [3] and TMeasy [8], could be accomplished using them for a simple caster-wheel model at the critical parameter domain of 'micro-shimmy'.

Acknowledgement

References

[1] H. Troger and K. Zeman, *A nonlinear-analysis of the generic types of loss of stability of the steady-state motion of a tractor-semitrailer*, Veh. Syst. Dyn. 13 (1984), pp. 161–172.
[2] D. Fratila and J. Darling, *Simulation of coupled car and caravan handling behaviour*, Veh. Syst. Dyn. 26 (1996), pp. 397–429.
[3] H.B. Pacejka, *Tyre and Vehicle Dynamics*, Elsevier Butterworth-Heinemann, Oxford, 2002.
[4] R.S. Sharp and M.A.A. Fernańdez, *Car-caravan snaking – part 1: The influence of pintle pin friction*, Proc. Inst. Mech. Eng. C, J. Mech. Eng. Sci. 216(7) (2002), pp. 707–722.
[5] A.L. Schwab and J.P. Meijaard, *Dynamics of flexible multibody systems having rolling contact: Application of the wheel element to the dynamics of road vehicles*, Veh. Syst. Dyn. 33 (1999), pp. 338–349.
[6] M. Gipser, *FTire – the tire simulation model for all applications related to vehicle dynamics*, Veh. Syst. Dyn. 45 (2007), pp. 139–151.
[7] C. Oertel and A. Fandre, *Ride comfort simulations and steps towards life time calculations: RMOD-K and ADAMS*, International ADAMS Users' Conference, Berlin, Germany, 1999.
[8] W. Hirschberg, G. Rill, and H. Weinfurter, *Tire model TMeasy*, Veh. Syst. Dyn. 45 (2007), pp. 101–119.
[9] P. Lugner, H.B. Pacejka, and M. Plöchl, *Recent advances in tyre models and testing procedures*, Veh. Syst. Dyn. 43 (2005), pp. 413–426.
[10] FEHRL, *Tyre/road noise*, Final report for the European Commission, SI2.408210, 2006.
[11] U. Sandberg and J. Ejsmont, *Tyre/Road Noise Reference Book*, Informex, Kisa, Sweden, 2002.

[12] P.B.U. Andersson and W. Kropp, *Rapid tyre/road separation: An experimental study of adherence forces and noise generation*, Wear 266 (2009), pp. 129–138.

[13] F. Gauterin and C. Ropers, *Modal tyre models for road noise improvement*, Veh. Syst. Dyn. 43 (2005), pp. 297–304.

[14] M.J.P. Miege and A.A. Popov, *The rolling resistance of truck tyres under a dynamic vertical load*, Veh. Syst. Dyn. 43 (2005), pp. 135–144.

[15] D. Takács, G. Orosz, and G. Stépán, *Delay effects in shimmy dynamics of wheels with stretched string-like tyres*, Eur. J. Mech. A, Solids 28 (2009), pp. 516–525.

[16] D. Takács and G. Stépán, *Experiments on quasiperiodic wheel shimmy*, J. Comput. Nonlinear Dyn. 4(3) (2009), pp. 1–7.

[17] B. von Schlippe and R. Dietrich, *Das Flattern Eines Bepneuten Rades (Shimmying of a pneumatic wheel)*, in *Bericht 140 der Lilienthal-Gesellschaft für Luftfahrtforschung*, 1941, pp. 35–45, 63–66 (English translation is available in NACA Technical Memorandum 1365, 1954, pp. 125–166, 217–228).

[18] L. Segel, *Force and moment response of pneumatic tires to lateral motion inputs*, J. Eng. Ind. Trans. ASME 88B (1966), pp. 37–44.

[19] H.B. Pacejka, *The Wheel Shimmy Phenomenon*, Technical University of Delft, The Netherlands, 1966.

[20] R.S. Sharp, S. Evangelou, and D.J.N. Limebeer, *Advances in the modelling of motorcycle dynamics*, Multibody Syst. Dyn. 12 (2004), pp. 251–283.

[21] P. Thota, B. Krauskopf, and M. Lowenberg, *Interaction of torsion and lateral bending in aircraft nose landing gear shimmy*, Nonlinear Dynam. 57 (2009), pp. 455–467.

[22] G. Stépán, *Delay, nonlinear oscillations and shimmying wheels*, Proceedings of Symposium CHAOS'97, Kluwer Ac. Publ., Dordrecht, Ithaca, NY, 1998, pp. 373–386.

[23] G. Heinrich and M. Klüppel, *Rubber friction, tread deformation and tire traction*, Wear 265 (2008), pp. 1052–1060.

[24] D. Takács and G. Stépán, *Nonlinear oscillations at critical shimmy parameters – experiments and numerics*, Proceedings of IMECE 2010, paper No. IMECE2010-38375, Vancouver, British Columbia, Canada, 2010, pp. 1–9.

[25] G. Stépán, *Retarded Dynamical Systems*, Longman Scientific and Technical, Essex, England, 1989.

[26] O. Duke, *Planet bike – radical thriller or flawed killer*, Bike 39(June) (1997), pp. 14–17.

[27] G. Somieski, *Shimmy analysis of simple aircraft nose landing gear model using different mathematical methods*, Aerosp. Sci. Technol. 8 (1997), pp. 545–555.

[28] P.D. Lax and B. Wendroff, *Systems of conservation laws*, Comm. Pure Appl. Math. 13 (1960), pp. 217–237.

[29] T. Kármán and M.A. Biot, *Mathematical Methods in Engineering*, McGraw-Hill Book Company, Inc., New York, 1940.

[30] D. Takács, *Dynamics of Towed Wheels – Nonlinear Theory and Experiments*, Budapest University of Technology and Economics, Hungary, 2010.

[31] D. Takács and G. Stépán, *Experimental modal analysis of towed elastic tyres during rolling*, in *Non-smooth Problems in Vehicle Systems Dynamics*, P.G. Thomsen and H. True, eds., Springer, Dordrecht, 2010, pp. 149–159.

[32] R.I. Leine, *Bifurcations of equilibria in non-smooth continuous systems*, Phys. D 223 (2006), pp. 121–137.